Orbit- and atom-resolved spin textures of intrinsic, extrinsic, and hybridized Dirac cone states

Lin Miao,[1,*] Z. F. Wang,[2,*] Meng-Yu Yao,[1] Fengfeng Zhu,[1] J. H. Dil,[3,4] C. L. Gao,[1] Canhua Liu,[1] Feng Liu,[2,†]
Dong Qian,[1,†] and Jin-Feng Jia[1,†]

[1]*Key Laboratory of Artificial Structures and Quantum Control (Ministry of Education), Department of Physics and Astronomy,*
Shanghai Jiao Tong University, Shanghai 200240, China
[2]*Department of Materials Science and Engineering, University of Utah, Salt Lake City, Utah 84112, USA*
[3]*Swiss Light Source, Paul Scherrer Institute, CH-5232 Villigen, Switzerland*
[4]*Physik-Institut, Universität Zürich-Irchel, 8057 Zürich, Switzerland*

Combining first-principles calculations and spin- and angle-resolved photoemission spectroscopy measurements, we identify the helical spin textures for three different Dirac cone states in the interfaced systems of a two-dimensional (2D) topological insulator (TI) of a Bi(111) bilayer and a three-dimensional (3D) TI Bi_2Se_3 or Bi_2Te_3. The spin texture is found to be the same for the intrinsic Dirac cone of Bi_2Se_3 or Bi_2Te_3 surface states, the extrinsic Dirac cone of Bi bilayer induced by the Rashba effect, and the hybridized Dirac cone between the former two states. Further orbit- and atom-resolved analysis shows that s and p_z orbits have a clockwise (counterclockwise) spin rotation tangent to the iso-energy contour of the upper (lower) Dirac cone, while p_x and p_y orbits have radial spin components. The Dirac cone states may reside on different atomic layers, but have the same spin texture. Our results suggest that the unique spin texture of Dirac cone states is a signature property of spin-orbit coupling, independent of topology.

One outstanding property that 3D TIs possess is the helical Dirac cone surface state residing inside a bulk gap, in which electron spin is locked with momentum [1,2]. This spin-momentum locking property makes TIs promising materials for realizing spintronic devices, because the electron backscattering is forbidden for nonmagnetic impurities. Therefore, understanding the spin texture of helical Dirac cone states is of fundamental interest with practical implication.

Experimentally, the helical spin texture of surface Dirac cone state of 3D TIs has been directly detected by spin- and angle-resolved photoemission spectroscopy (SARPES) [3–8]. It can also be manipulated through its interaction with polarized light [9,10]. Very recently it has been noted that because of the strong spin-orbit coupling (SOC), total angular momentum, spin plus orbital angular momentum, should be the good quantum number in TIs. Consequently, the spin texture of TIs is expected to be coupled with atomic orbits in a specific manner [11–13]. Both theory [11] and experiment [12,13] have shown some very interesting patterns of radial/tangential spin texture coupled with p orbits in the Bi_2Se_3 family.

Besides the "intrinsic" Dirac cone state of TIs, the "extrinsic" Dirac cone state may be generated by Rashba effect, such as the one formed when the Bi(111) bilayer is grown on the Bi_2Se_3 substrate [14,15]. Also, when the Bi(111) bilayer is grown on Bi_2Te_3 [14,16], a kind of hybridized Dirac cone state is formed between the intrinsic surface Dirac cone state of Bi_2Te_3 and the extrinsic Rashba Dirac cone state of Bi(111). These Dirac cone states are all associated with strong SOC. However, different from the intrinsic surface states of TI, which are topologically protected inside a bulk gap, the extrinsic and hybridized states have no topological origin, even though they

are formed by interfacing a 2D TI of Bi(111) bilayer [17–21] and a 3D TI of Bi_2Se_3 or Bi_2Te_3. It will be interesting to find out the spin texture of these nontopological Dirac states, in comparison with the topological surface Dirac states of 3D TIs.

In this work, the spin texture of three different Dirac cone states in the system of Bi/Bi_2Se_3 and Bi/Bi_2Te_3 are systemically studied. Both first-principles calculations and SARPES measurements show that the total spins form an identical helical spin texture for all three Dirac cones. Furthermore, the orbit-resolved calculations reveal that s and p_z orbits have a clockwise (counterclockwise) spin rotation tangent to the iso-energy contour of the upper (lower) Dirac cone, while p_x and p_y orbits have a radial spin component, in agreement with recent studies [11–13]. The atom-resolved calculations reveal that the Dirac cone states may reside on different atomic layers, but their spin texture remains the same.

Our first-principles calculations are carried out in the framework of generalized gradient approximation with a Perdew-Burke-Ernzerhof functional using the VASP package [22]. The lattice constants of the substrate are taken from experiments ($a = 4.138$ Å for Bi_2Se_3 and $a = 4.386$ Å for Bi_2Te_3), and the Bi(111) bilayer is strained to match the substrate lattice parameter. All calculations are performed with a plane-wave cutoff of 400 eV on an $11 \times 11 \times 1$ Monkhorst-pack k-point mesh. The substrate is modeled by a slab of 6 quintuple layer (QL) Bi_2Se_3 and Bi_2Te_3 because it takes 5–6 QLs to eliminate top-bottom surface interaction for the film to assume bulk property [23], and the vacuum layers are over 20 Å thick to ensure decoupling between neighboring slabs. We have also done test calculations using 8 QLs of Bi_2Se_3, which confirm that our results using 6 QLs are converged. During structural relaxation, atoms in the lower 4QL substrate are fixed in their respective bulk positions, and the Bi bilayer and upper 2QL of substrate are allowed to relax until the forces are smaller than 0.01 eV/Å.

---

*L.M. and Z.F.W. contributed equally to this work.

†Corresponding authors: fliu@eng.utah.edu; dqian@sjtu.edu.cn; jfjia@sjtu.edu.cn
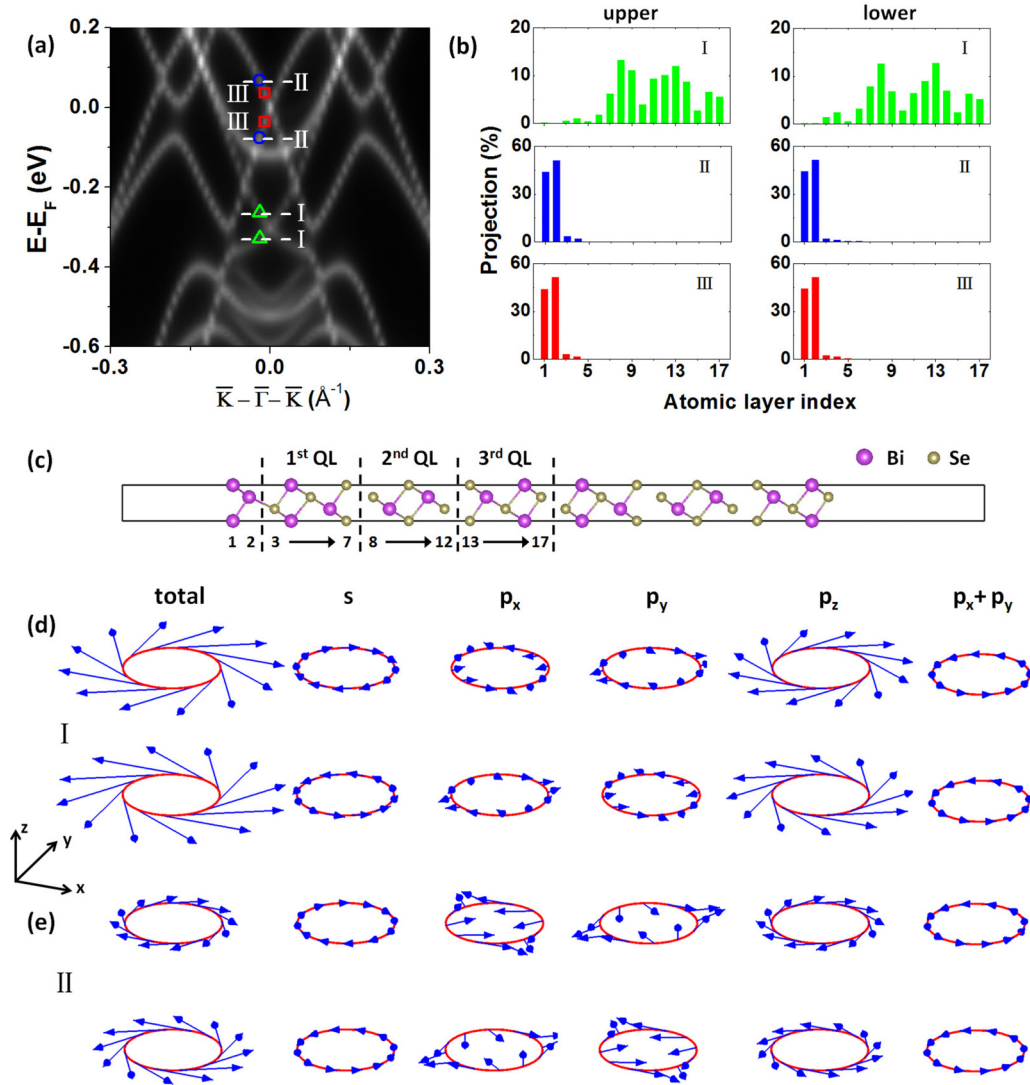
FIG. 1. (Color online) (a) Bi/Bi$_2$Se$_3$ spectral function projected onto a top Bi bilayer plus upper 2QL Bi$_2$Se$_3$. (b) Percentage contribution of different atoms to the Dirac cone states marked by labels I, II, and III with different colors and symbols in (a). Upper (lower) denotes upper (lower) Dirac cone states and the atomic layer index is shown in (c). (c) Atomic structure of the optimized Bi/Bi$_2$Se$_3$. A Bi bilayer and upper 3QL Bi$_2$Se$_3$ are labeled with numbers to denote their atomic layer index. (d) and (e) Orbit-resolved spin textures of the iso-energy contour Dirac cone state at the energy marked by labels I and II in (a).

First, we take a look at the Bi/Bi$_2$Se$_3$, where both intrinsic and extrinsic Dirac cone states coexist [14]. Figure 1(a) shows the spectral function of Bi/Bi$_2$Se$_3$ projected onto the Bi bilayer plus top 2QL of Bi$_2$Se$_3$. One sees two Dirac cones at the Γ point, one below and the other near the Fermi level. To reveal the origin of these two Dirac cones, we plot their real-space distribution by choosing three data points from the upper and lower Dirac cones, as marked by I, II, and III in Fig. 1(a). The corresponding momenta are -0.02, -0.02, and -0.01 Å^{-1} for I, II, and III states, respectively. The atom-projected state components are shown in Fig. 1(b), with the atomic layer indexes labeled in Fig. 1(c). The Dirac cone states below the Fermi level come almost completely from the substrate with little contribution from the Bi bilayer [Fig. 1(b), top panel]. This indicates that it is an intrinsic Dirac cone of Bi$_2$Se$_3$. The Dirac cone states near the Fermi level come predominantly from the top Bi bilayer, having little substrate contribution

[see Fig. 1(b), two bottom panels]. This indicates that it is an extrinsic Dirac cone generated by the Rashba splitting of Bi bilayer bands, as discussed before [14,15]. Additionally, we note that due to interfacial interaction with the Bi bilayer, the intrinsic surface Dirac cone has a wide real-space distribution in the second and third QL [Fig. 1(b), top panel] that peaks at the boundary between the first and second, and the second and third QL [i.e., the seventh and eighth, and 12th and 13th atomic layer as seen in Fig. 1(c)]. This is different from the surface Dirac cone of bare Bi$_2$Se$_3$ that decays from the first and second QL [24]. The Bi bilayer pushes down and broadens the surface states of Bi$_2$Se$_3$. This is consistent with the recent findings by Wu *et al.* that the vertical location of the surface Dirac cone state of a 3D TI can be tuned by depositing a layer of conventional insulator [25].

Although the two Dirac cones in Fig. 1(a) have different physical origins, their spin textures are found to be the same.
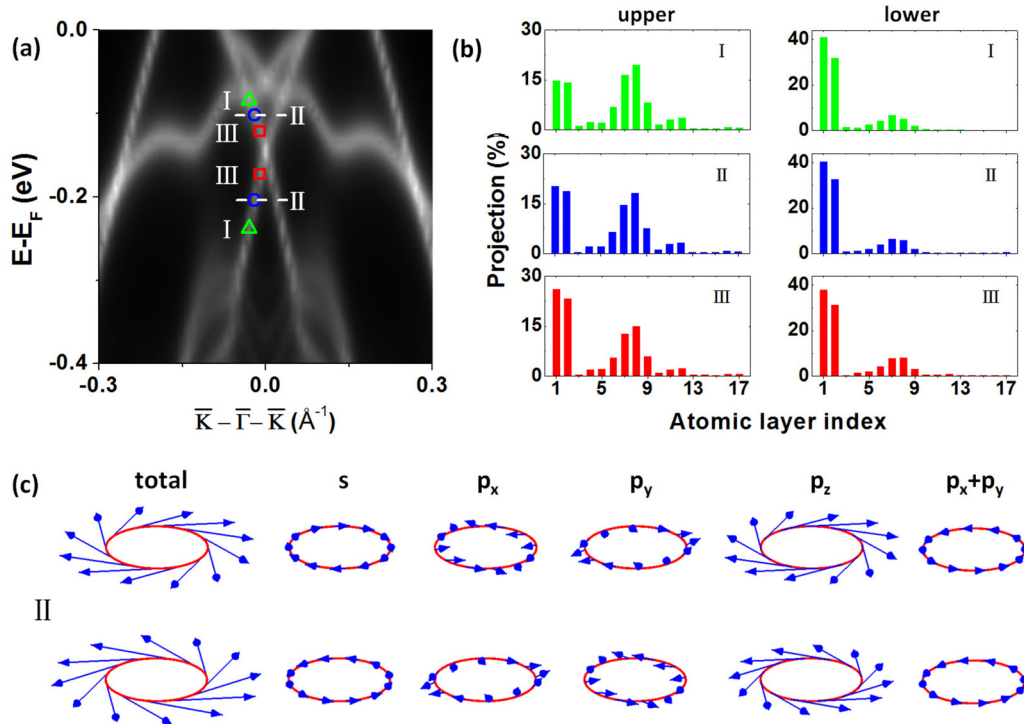
FIG. 2. (Color online) (a) Bi/Bi$_2$Te$_3$ spectral function projected onto the top Bi bilayer plus upper 1QL Bi$_2$Te$_3$. (b) Percentage contribution of different atoms to the Dirac cone states marked by labels I, II, and III with different colors and symbols in (a). (c) Orbit-resolved spin textures of the iso-energy contour Dirac cone state at the energy marked by label II in (a). The scaling factor of the arrow length is the same as that in Fig. 1.

The total and orbit-resolved spin textures along the iso-energy contour at the energy marked by I (intrinsic Bi$_2$Se$_3$ Dirac cone) and II (extrinsic Bi Dirac cone) are shown in Figs. 1(d) and 1(e), respectively. The total spins of both Dirac cones are oriented clockwise (counterclockwise) in the upper (lower) Dirac cone. s and p_z orbits have the same helical spin texture as the total spin, but p_x and p_y orbits have a different spin texture with additional radial spin component, pointing toward opposite directions along the 135° or 45° axis. In addition, p_x orbit spin texture in the upper (lower) Dirac cone is the same as p_y orbit spin texture in the lower (upper) Dirac cone. These in-plane p orbit spin textures are consistent with the theoretical model prediction by Zhang *et al.* [11]. We note that although both p_x and p_y orbit spins have radial components, their summation, $p_x + p_y$ orbit spins is helical becoming tangent to iso-energy contour, albeit they are oriented counterclockwise in both upper and lower Dirac cones [see Figs. 1(d) and 1(e)]. The total helical in-plane p orbit spins with the same orientation in the upper and lower Dirac cones have been recently experimentally observed in the Bi$_2$Se$_3$ surface Dirac cones [13]. The only difference between the spin textures of intrinsic and extrinsic Dirac cones is the spin magnitude. For the intrinsic Dirac cone, the amplitude of s, p_x, and p_y orbit spins are negligible, and the magnitude of p_z orbit spin is the largest. While for the extrinsic Dirac cone, the amplitude of s orbit spin is negligible, and the magnitude of three p orbit spins are comparable to each other.

Next, we turn to the Bi/Bi$_2$Te$_3$ where hybridized Dirac cone states arise [14]. Figure 2(a) shows the spectral function of Bi/Bi$_2$Te$_3$ projected onto a Bi bilayer plus upper 1QL Bi$_2$Te$_3$.

There appears only one Dirac cone at the Γ point below Fermi level. Similar to the case of Bi/Bi$_2$Se$_3$, three groups of data points are chosen around this Dirac cone, as marked by I, II, and III in Fig. 2(a). The corresponding momenta are −0.03, −0.02, and −0.01 Å^{-1} for I, II, and III states, respectively. The atom-projected components of these states are shown in Fig. 2(b), and the atomic layer indexes are the same as those shown in Fig. 1(c). One major difference from Bi/Bi$_2$Se$_3$ is that the only one Dirac state in Bi/Bi$_2$Te$_3$ has sizable contributions from both a Bi bilayer and Bi$_2$Te$_3$ substrate, as clearly seen from Fig. 2(b). This indicates that it is a hybridized Dirac state between the intrinsic surface Dirac state of Bi$_2$Te$_3$ and the extrinsic Rashba Dirac state of the Bi bilayer. A previous study has further shown another interesting point that such hybridization might enhance many-body interaction within the Dirac states [14]. Figure 2(b) also shows that the hybridization in the upper Dirac cone is stronger than that in the lower Dirac cone. Moving away from the Dirac point (from III to I), the components of the Bi bilayer (Bi$_2$Te$_3$ substrate) decreases (increases) in the upper Dirac cone, but they show little change in the lower Dirac cone. The substrate contribution to the Dirac cone is not localized in the first QL but between the first and second QL [i.e., the sixth to ninth atomic layer as seen in Fig. 1(c)]. This is because the surface state is pushed slightly away from the Bi/Bi$_2$Te$_3$ interface compared to the bare Bi$_2$Te$_3$ surface state [8]. The spin textures of this hybridized Dirac cone state along the iso-energy contour at the energy marked by label II are shown in Fig. 2(d). The total and orbit-resolved spin textures of the hybridized Dirac cone are the same as those in the intrinsic and extrinsic Dirac cones of the Bi/Bi$_2$Se$_3$
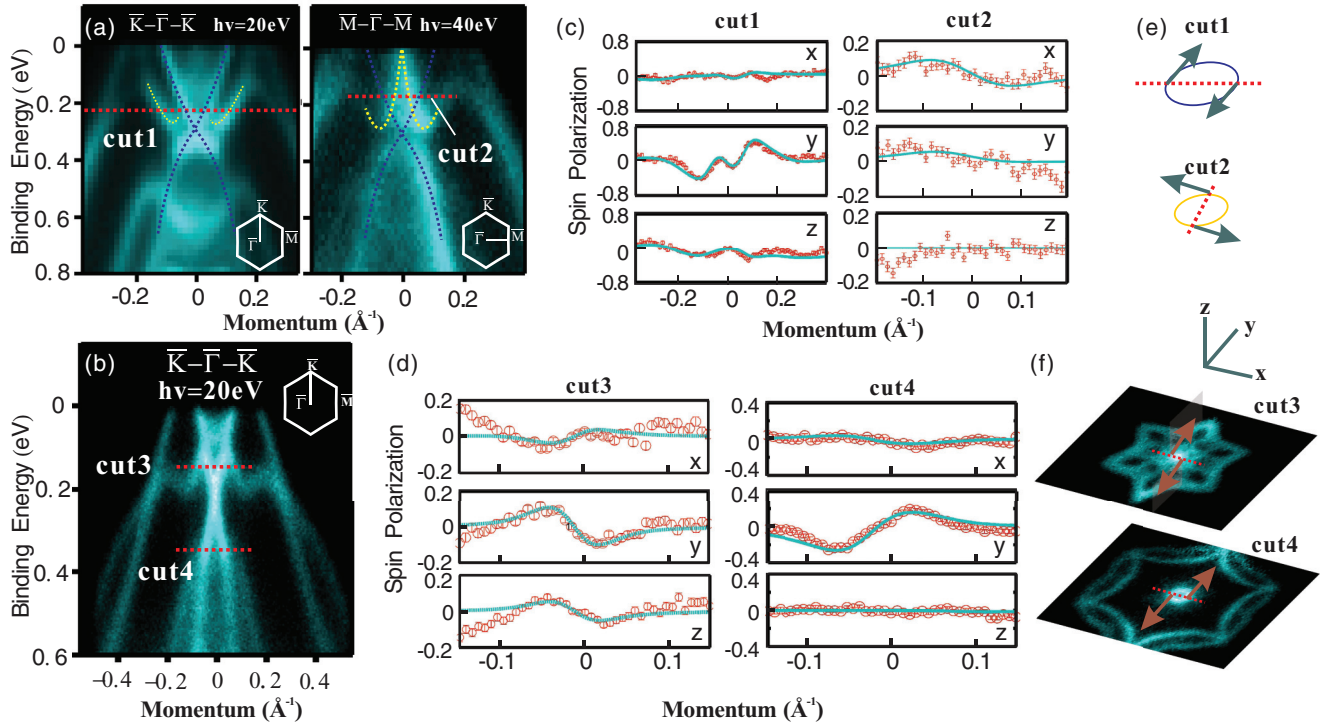
FIG. 3. (Color online) (a) Spin-integrated ARPES spectra of Bi/Bi$_2$Se$_3$ and (b) Bi/Bi$_2$Te$_3$. The dashed blue and yellow lines show the position of the intrinsic and extrinsic Dirac cones. Experimentally, the relative intensity of two Dirac cones can be tuned by incident photon energy. (c) and (d) The experimental momentum dependent spin polarization and fitting data of Bi/Bi$_2$Se$_3$ and Bi/Bi$_2$Te$_3$. (e) and (f) Spin textures of intrinsic, extrinsic Dirac cones, and hybridized Dirac cone. The images in (f) are the constant energy contours of ARPES intensity.

system. s and p_z orbits have a helical spin texture, while p_x and p_y orbits have a nonhelical radial spin component.

We can conclude from the above calculation results several common features for the three different Dirac cone states. (1) The total spins have a helical spin texture, which is clockwise (counterclockwise) in the upper (lower) Dirac cone. (2) s and p_z orbit spins have the same texture as to the total spins. (3) p_x and p_y orbit spins have a radial spin component individually, but their sum becomes helical. (4) The substrate surface state is pushed down away from the first QL by the presence of the Bi bilayer.

To support our first-principles calculations, we have measured the total spin textures of these Dirac cone states in the Bi/Bi$_2$Se$_3$ and Bi/Bi$_2$Te$_3$ systems by SARPES. The method for epitaxially growing high quality Bi/Bi$_2$Te$_3$ and Bi/Bi$_2$Se$_3$ samples is the same as our previous works [14,21]. SARPES measurements were performed at the SIS beam line at the Swiss Light Source using the COPHEE spectrometer with two 40 kV classical Mott detectors. The typical energy and momentum resolution was 50 meV and 3% of the surface Brillouin zone at SIS. All the measurements were carried out at 30 K in ultrahigh vacuum with a base pressure better than 1×10^{-10} torr. Proper measurement geometries were used to minimize SARPES matrix elements effects. For all measurements, p-polarized incident light was used to minimize the additional effect found in Ref. [10] as much as possible. For the Bi/Bi$_2$Se$_3$ system, the relative spectra intensity of the two Dirac cone states can be tuned by using different photon energies. As shown in Fig. 3(a), the intrinsic Dirac cone of Bi$_2$Se$_3$ was observed clearly with photon energy

of 20 eV and the extrinsic Dirac cone of the Bi bilayer was detected with photon energy of 40 eV.

Figure 3(a) shows the spin-integrated ARPES spectra of Bi/Bi$_2$Se$_3$ along $\bar{K}$-$\bar{\Gamma}$-$\bar{K}$ and $\bar{M}$-$\bar{\Gamma}$-$\bar{M}$ directions, in which one can see both intrinsic and extrinsic Dirac cones. In the SARPES measurements, two spin-resolved momentum distribution curves (MDC) were taken [cut1 and cut2, as shown by the horizontal dashed lines in Fig. 3(a)]. Cut1 is at 220 meV below the Fermi level to study the intrinsic Dirac cone, and cut2 is at 180 meV below the Fermi level to study the extrinsic Dirac cone. The spin polarization is extracted by using the the two-step fitting routine of SARPES data [3,26,27]. The momentum dependent spin polarization and fitting data are shown in Fig. 3(c), from which we extract the spin textures. Figure 3(e) presents the spin textures of intrinsic and extrinsic Dirac cones, which is clockwise in the upper intrinsic Dirac cone and counterclockwise in the lower extrinsic Dirac cone. For both Dirac cones, spins are nearly in-plane polarized. Figure 3(b) shows the spin-integrated ARPES spectra of Bi/Bi$_2$Te$_3$ along $\bar{K}$-$\bar{\Gamma}$-$\bar{K}$ direction, in which one can see the hybridized Dirac cone. Similar to the SARPES measurement for Bi/Bi$_2$Se$_3$, we also take two MDC cuts (cut3 and cut4), as shown by the dashed lines in Fig. 3(b). Cut3 (cut4) is taken at 150 (350) meV below the Fermi level, slightly above (below) the hybridized Dirac cone. The polarization and fitting data are shown in Fig. 3(d). As shown in Fig. 3(f), the spin texture is clockwise and counterclockwise in the upper and lower Dirac cone, respectively. We note that using our experimental configuration, the complexity in SARPES measurements on TI materials [10] is largely suppressed.
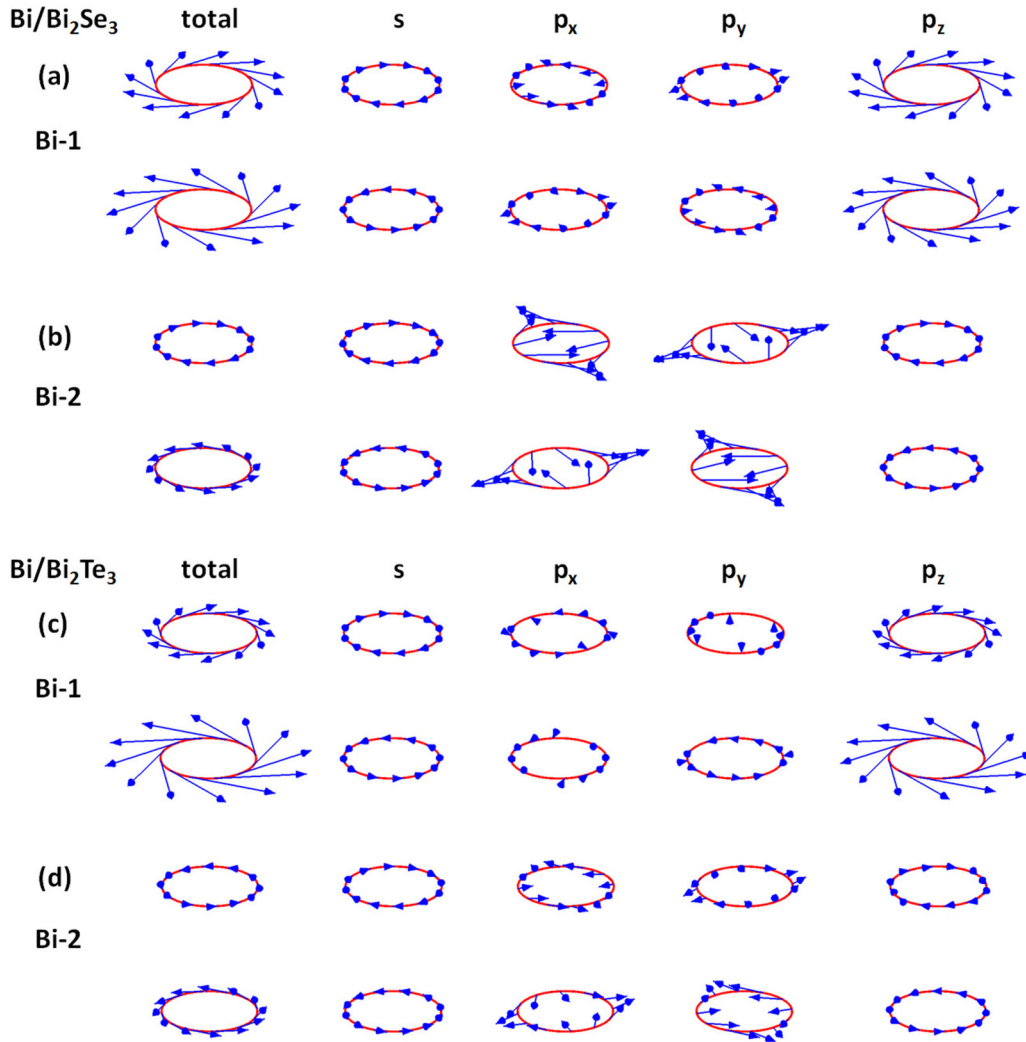
FIG. 4. (Color online) Atom- and orbit-resolved spin textures of the iso-energy contour Dirac cone state at the energy marked by label II in Figs. 1(a) and 2(a). (a) and (b) The spin textures of the first (Bi-1) and second (Bi-2) atom in Bi/Bi$_2$Se$_3$. (c) and (d) The spin textures of the first (Bi-1) and second (Bi-2) atom in Bi/Bi$_2$Te$_3$. The scaling factor of the arrow length is twice that in Fig. 1.

The measured spin orientation should mostly reflect the spin orientation in its *initio* states. Thus, to a large degree, our SARPES measurements indicated that all three Dirac cones have the same helical spin textures, independent of topology, consistent with our first-principle calculations.

Lastly, we present additional first-principles calculations to show the orbit- and atom-resolved spin textures of the Dirac cone states. Here we will focus on the top two Bi atoms. Overall, except the spin magnitude, the atom-resolved spin textures have the same structure compared to the spin textures by adding all atoms together, as shown in Fig. 4. However, from the atom projection, we can obtain some detailed local information of spin texture by considering the spin magnitude difference. Figures 4(a) and 4(b) are the spin textures of the extrinsic Dirac cone projected onto the top two Bi atoms of Bi/Bi$_2$Se$_3$. We can see that the spin magnitude is very different between the two Bi atoms. For the Bi-1 atom, p_z orbit spin has the largest magnitude, while s, p_x, and p_y orbit spins are negligible. But for the Bi-2 atom, p_x and p_y orbit spins have the largest magnitude, while s and p_z orbit spins are negligible.

Figures 4(c) and 4(d) are the spin textures of the hybridized Dirac cone projected onto the top two Bi atoms of Bi/Bi$_2$Te$_3$. The atom-resolved spin textures of the hybridized Dirac cone are similar to those in the extrinsic Dirac cone. We have also checked the atom-resolved spin textures for the intrinsic Dirac cone, which are again similar.

In summary, we have identified the helical spin textures for three different Dirac cone states in the interfaced systems of Bi/Bi$_2$Se$_3$ and Bi/Bi$_2$Te$_3$, from first-principles calculations and experiments. We confirm the recent theory [11] and experiment [12,13] that the spin texture of intrinsic surface Dirac cone states of 3D TIs is coupled with orbit, resulting in an overall spin-orbit texture. Characteristically, s and p_z orbits have the conventional helical spin texture; p_x and p_y orbits show individually radial spin component, while the sum of the two shows a total in-plane helical spins. We further show that the same spin texture is also applicable to the extrinsic Rashba Dirac cone states of the Bi(111) bilayer on a substrate as well as to the hybridized Dirac cone states between a TI surface state and a thin-film Rashba state. Therefore, we suggest that

[1] M. Z. Hasan and C. L. Kane, Rev. Mod. Phys. **82**, 3045 (2010).

[2] X.-L. Qi and S.-C. Zhang, Rev. Mod. Phys. **83**, 1057 (2011).

[3] D. Hsieh, Y. Xia, L. Wray, D. Qian, A. Pal, J. H. Dil, J. Osterwalder, F. Meier, G. Bihlmayer, C. L. Kane, Y. S. Hor, R. J. Cava, and M. Z. Hasan, Science **323**, 919 (2009).

[4] D. Hsieh, Y. Xia, D. Qian, L. Wray, J. H. Dil, F. Meier, J. Osterwalder, L. Patthey, J. G. Checkelsky, N. P. Ong, A. V. Fedorov, H. Lin, A. Bansil, D. Grauer, Y. S. Hor, R. J. Cava, and M. Z. Hasan, Nature (London) **460**, 1101 (2009).

[5] P. Roushan, J. Seo, C. V. Parker, Y. S. Hor, D. Hsieh, D. Qian, A. Richardella, M. Z. Hasan, R. J. Cava, and A. Yazdani, Nature (London) **460**, 1106 (2009).

[6] Z.-H. Pan, E. Vescovo, A. V. Fedorov, D. Gardner, Y. S. Lee, S. Chu, G. D. Gu, and T. Valla, Phys. Rev. Lett. **106**, 257004 (2011).

[7] S. Souma, K. Kosaka, T. Sato, M. Komatsu, A. Takayama, T. Takahashi, M. Kriener, K. Segawa, and Y. Ando, Phys. Rev. Lett. **106**, 216803 (2011).

[8] S. V. Eremeev, G. Landolt, T. V. Menshchikova, B. Slomski, Y. M. Koroteev, Z. S. Aliev, M. B. Babanly, J. Henk, A. Ernst, L. Patthey, A. Eich, A. A. Khajetoorians, J. Hagemeister, O. Pietzsch, J. Wiebe, R. Wiesendanger, P. M. Echenique, S. S. Tsirkin, I. R. Amiraslanov, J. H. Dil, and E. V. Chulkov, Nat. Commun. **3**, 635 (2012).

[9] C.-H. Park and S. G. Louie, Phys. Rev. Lett. **109**, 097601 (2012).

[10] C. Jozwiak, C.-H. Park, K. Gotlieb, C. Hwang, D.-H. Lee, S. G. Louie, J. D. Denlinger, C. R. Rotundu, R. J. Birgeneau, Z. Hussain, and A. Lanzara, Nat. Phys. **9**, 293 (2013).

[11] H. Zhang, C.-X. Liu, and S.-C. Zhang, Phys. Rev. Lett. **111**, 066801 (2013).

[12] Y. Cao, J. A. Waugh, X.-W. Zhang, J.-W. Luo, Q. Wang, T. J. Reber, S. K. Mo, Z. Xu, A. Yang, J. Schneeloch, G. D. Gu, M. Brahlek, N. Bansal, S. Oh, A. Zunger, and D. S. Dessau, Nat. Phys. **9**, 499 (2013).

[13] Z. Xie, S. He, C. Chen, Y. Feng, H. Yi, A. Liang, L. Zhao, D. Mou, J. He, Y. Peng, X. Liu, Y. Liu, G. Liu, X. Dong, L. Yu, J. Zhang, S. Zhang, Z. Wang, F. Zhang, F. Yang *et al.*, Nat. Commun. **5**, 3382 (2014).

[14] L. Miao, Z. F. Wang, W. Ming, M.-Y. Yao, M.-X. Wang, F. Yang, Y. R. Song, F. Zhu, A. V. Fedorov, Z. Sun, C. L. Gao, C. Liu, Q.-K. Xue, C.-X. Liu, F. Liu, D. Qian, and J.-F. Jia, Proc. Natl. Acad. Sci. USA **110**, 2758 (2013).

[15] Z. F. Wang, M.-Y. Yao, W. Ming, L. Miao, F. Zhu, C. Liu, C. L. Gao, D. Qian, J.-F. Jia, and F. Liu, Nat. Commun. **4**, 1384 (2013).

[16] T. Hirahara, G. Bihlmayer, Y. Sakamoto, M. Yamada, H. Miyazaki, S.-i. Kimura, S. Blügel, and S. Hasegawa, Phys. Rev. Lett. **107**, 166801 (2011).

[17] S. Murakami, Phys. Rev. Lett. **97**, 236805 (2006).

[18] Z. Liu, C.-X. Liu, Y.-S. Wu, W.-H. Duan, F. Liu, and J. Wu, Phys. Rev. Lett. **107**, 136805 (2011).

[19] L. Chen, Z. F. Wang, and F. Liu, Phys. Rev. B **87**, 235420 (2013).

[20] Z. F. Wang, L. Chen, and F. Liu, arXiv:1402.6754.

[21] F. Yang, L. Miao, Z. F. Wang, M.-Y. Yao, F. Zhu, Y. R. Song, M.-X. Wang, J.-P. Xu, A. V. Fedorov, Z. Sun, G. B. Zhang, C. Liu, F. Liu, D. Qian, C. L. Gao, and J.-F. Jia, Phys. Rev. Lett. **109**, 016801 (2012).

[22] G. Kresse and J. Hafner, Phys. Rev. B **47**, 558 (1993).

[23] Y. Zhang, K. He, C.-Z. Chang, C.-L. Song, L.-L. Wang, X. Chen, J.-F. Jia, Z. Fang, X. Dai, W.-Y. Shan, S.-Q. Shen, Q. Niu, X.-L. Qi, S.-C. Zhang, X.-C. Ma, and Q.-K. Xue, Nat. Phys. **6**, 584 (2010).

[24] W. Zhang, R. Yu, H.-J. Zhang, X. Dai, and Z. Fang, New J. Phys. **12**, 065013 (2010).

[25] G. Wu, H. Chen, Y. Sun, X. Li, P. Cui, C. Franchini, J. Wang, X.-Q. Chen, and Z. Zhang, Sci. Rep. **3**, 1233 (2013).

[26] F. Meier, H. Dil, J. Lobo-Checa, L. Patthey, and J. Osterwalder, Phys. Rev. B **77**, 165431 (2008).

[27] J. H. Dil, J. Phys.: Condens. Matter **21**, 403001 (2009).